

• Original Paper •

Microphysical Processes of a Stratiform Precipitation Event over Eastern China: Analysis Using Micro Rain Radar data

Hong WANG^{1,2,3}, Hengchi LEI^{*1}, and Jiefan YANG¹

¹Key Laboratory of Cloud-Precipitation Physics and Severe Storms, Institute of Atmospheric Physics, Chinese Academy of Sciences, Beijing 100029, China

²University of Chinese Academy of Sciences, Beijing 100040, China

³Shandong Weather Modification Office, Jinan 250031, China

(Received 11 January 2017; revised 3 May 2017; accepted 6 June 2017)

ABSTRACT

Data collected using the micro rain radar (MRR) situated in Jinan city, eastern China, were used to explore the altitudinal and temporal evolution of rainfall microphysical characteristics, and to analyze the bright band (BB) characteristics and hydrometeor classification. Specifically, a low-intensity and stable stratiform precipitation event that occurred from 0000 to 0550 UTC 15 February 2015 and featured a BB was studied. During this event, the rainfall intensity was less than 2 mm h^{-1} at a height of 300 m, which was above the radar site level, so the errors caused by the vertical air motion could be ignored. The freezing height from the radiosonde matched well with the top of the BB observed by the MRR. It was also found that the number of 0.5–1 mm diameter drops showed no noticeable variation below the BB. The maximum fall velocity and the maximum gradient fall velocity (GFV) of the raindrops appeared at the bottom of the BB. Meanwhile, a method that uses the GFV and reflectivity to identify the altitude and the thickness of the BB was established, with which the MRR can provide a reliable and real-time estimation of the 0°C isotherm. The droplet fall velocity was used to classify the types of snow crystals above the BB. In the first 20 min of the selected precipitation event, graupel prevailed above the BB; and at an altitude of 2000 m, graupel also dominated in the first 250 min. After 150 min, the existence of graupel and dendritic crystals with water droplets above the BB was inferred.

Key words: drop size distribution, micro rain radar, bright band, microphysical processes

Citation: Wang, H., H. C. Lei, and J. F. Yang, 2017: Microphysical processes of a stratiform precipitation event over eastern China: analysis using micro rain radar data. *Adv. Atmos. Sci.*, **34**(12), 1472–1482, <https://doi.org/10.1007/s00376-017-7005-6>.

1. Introduction

The evolution of precipitation has been extensively discussed in past research (Srivastava, 1971; Gossard et al., 1990; Hu and Srivastava, 1995; Harikumar et al., 2009, 2010). Raindrops are simultaneously forced by buoyancy, gravity and air drag while falling, causing collisional breakup, coalescence, evaporation and other microphysical processes. An understanding of the altitudinal and temporal microphysical structure of precipitation is very useful in microwave communication, radar meteorology, satellite meteorology, soil erosion and cloud physics (Harikumar et al., 2009). As a basic rain microphysical feature, drop size distribution (DSD) is a common but key parameter for describing a precipitation event. DSD varies with time and space due to the complexity of the atmospheric and climatological system. At the micro level, the processes of coalescence and break-up

may be major factors controlling DSD (Srivastava, 1971). DSD information is useful for meteorological research, such as investigating hydrometeor characteristics and precipitation microphysical processes, and validating microphysical parameterization schemes in numerical prediction models to improve the accuracy of weather forecasts (Brandes et al., 2004). Knowledge of DSD is also crucial for radar quantitative precipitation estimation, while the shapes of DSD determine the relationship between radar reflectivity and the rainfall intensity (Atlas et al., 1973; Doelling et al., 1998).

Nevertheless, most previous studies have been conducted on probes installed on surficial disdrometers or aircraft. A disdrometer is a common instrument used to measure surficial DSDs, as the instrument can be operated continuously and can withstand weather hazards. However, the disdrometer sampling area is near the ground, lacking spatial detection unless a number of instruments arranged in an intense network are working concurrently. It is difficult to determine the altitudinal variation of DSD using disdrometers only; plus, DSD observations by probes mounted on aircraft are limited

* Corresponding author: Hengchi LEI
Email: leihc@mail.iap.ac.cn

to areas where the aircrafts can fly, resulting in discontinuous sampling data both temporally and spatially.

Besides, for radar quantitative precipitation estimation, the existence of a bright band (BB) always leads to an overestimation of R in stratiform precipitation when the Z/R relation is used (Rico-Ramirez et al., 2005, Cha et al., 2009), where R is the rain rate and Z the reflectivity factor. So, the identification of the BB is an important step when trying to correct the large positive biases of radar reflectivity that it causes. Meanwhile, another important factor for radar quantitative precipitation estimation is the type of hydrometeors within the radar beam (Rico-Ramirez et al., 2005). Towards this goal, the classification of hydrometeors may be a useful step.

Among the instruments developed that can provide DSD data spatially and continuously, wind profile radar (WPR) and micro rain radar (MRR) are increasingly popular. Compared with WPR, an MRR can be compactly built and operate with a transmission power as small as 50 mW. In the present study, we focused on understanding the altitudinal and temporal variation of the microphysical structure during a single precipitation event with a BB, and the potential of MRR to identify the BB and classify hydrometeors. Furthermore, few measurements of this nature have been made in eastern China, so analysis of the datasets obtained with the MRR in the present work, which operates from the roof of Shandong Weather Modification Office, Jinan (36°41'N, 116°59'E), China, also helps to fill this knowledge gap. Specifically, an event that lasted for 350 min on 15 February 2015 was examined. The rain DSDs, R , equivalent radar reflectivity factor (Z_e) and fall velocity (v_m) retrieved by the MRR were studied.

The paper is organized as follows: A brief description of the MRR and its retrieval procedures are provided in section 2. Section 3 details the data availability. Section 4 analyzes the data, based on the key parameters mentioned above (R, Z_e, v_m , DSD etc.), and proposes the methods to identify the BB. The potential to classify hydrometeors from the MRR measurements is also discussed. Further discussion and conclusions are provided in section 5.

2. Overview of the MRR

2.1. General features

The MRR operates at 24.23 GHz and is a low-cost, vertically pointing Doppler radar. The manufacturer is a German company called Meteorologische mess Technik GmbH (METEK) (Harikumar et al., 2012) — see www.metek.de for more information. The MRR requires low transmission power (only 50 mW), and one radar antenna can be used with the MRR without beam overlap problems (Peters et al., 2005). Moreover, small amounts of precipitation — beyond the capabilities of conventional rain gauges — can be detected by the MRR. The MRR system specification used in the present study is detailed in Table 1. In this study, the temporal resolution was 60 s and the altitudinal resolution was

100 m.

2.2. Retrieval procedures

The reflectivity spectra used in our work have been corrected for the noise floor and for attenuation (METEK, 2017). Techniques for attenuation correction of MRR echoes from droplets, including the method adopted for the MRR, are discussed in detail in Peters et al. (2010). The retrieval procedures of the MRR have been described in detail previously by Peters et al. (2002) and Kirankumar and Kunhikrishnan (2013). Briefly, to derive the DSD, Gunn and Kinzer (1949) proposed the relationship between the falling velocity v of droplets and the diameter D of particles, which was put into analytical form by Atlas et al. (1973):

$$D(v, h) = \frac{1}{0.6} \ln \frac{10.3}{9.65 - v/\delta_v(h)}. \quad (1)$$

Here, the diameter of particles D is in mm, and $0.109 \leq D \leq 5.8$ mm; and v is in m s^{-1} . Equation (1) also holds for liquid droplets. Under the assumption of the U.S. Standard Atmosphere (1976 conditions), Foote and Du Toit (1969) found the relation $v \propto \rho^{-0.4}$ where ρ is the density of water, meaning v can be corrected approximately as a function of height h (Peters et al., 2005):

$$\delta_v(h) = [1 + 3.68 \times 10^{-5}h + 1.71 \times 10^{-9}h^2]. \quad (2)$$

The DSD can then be derived from the spectral reflectivity density $\eta(D, h)$ and single particle backscattering cross section $\sigma(D)$:

$$N(D, h)\Delta D = \frac{\eta(D, h)}{\sigma(D)}\Delta D, \quad (3)$$

where $N(D, h)$ is the number density of particles. Then, from the retrieved DSD, the radar reflectivity factor Z is obtained:

$$Z = \int_{D_{\min}}^{D_{\max}} N(D)D^6 dD. \quad (4)$$

Table 1. Specification of the MRR.

Specification of the MRR	
Transmitting frequency	24.23 GHz (K-band)
Wavelength	12.38 mm
Transmitting power	50 mW
Receiver–transmitter antenna	Offset-parabolic; diameter: 0.6 m
Beam width	2°
Modulation	FM-CW (frequency-modulated continuous wave)
Temporal resolution	10–3600 s (adjustable)
Altitudinal resolution	10–1000 m; typical values in the range 30–100 m (adjustable)
No. of range gates	31
Spectral velocity resolution	0.1905 m s^{-1}
Velocity range	0–12.192 m s^{-1}
Diameter range	0.109–6 mm
Height range	Up to 6000 m with 31 range gates
Dimensions	0.6 m × 0.6 m × 0.6 m

Assuming stagnant air, v can be identified using the raindrop falling velocity. So, one of the main error sources and limitations is that the retrieval method does not account for the deviation caused by vertical air motion and turbulence (Prat and Barros, 2010).

Transformation of Eq. (1) gives us

$$v(D) = (9.65 - 10.3 \exp(-0.6D))\delta_v(h), \quad (5)$$

where the units of $v(D)$ are m s^{-1} , and the units for the diameter D are mm. Profiles of the rain rate R , Eq. (6), liquid water content (LWC), Eq. (7) (Das et al., 2010), can be computed as follows:

$$R = \frac{\pi}{6} \int_{D_{\min}}^{D_{\max}} N(D)v(D)D^3 dD, \quad (6)$$

$$\text{LWC} = \rho_w \frac{\pi}{6} \int_{D_{\min}}^{D_{\max}} N(D)D^3 dD. \quad (7)$$

Instead of the Z/R and LWC being derived from $N(D)$, the Z_e and v_m are calculated by integrating the Doppler spectrum directly (Maahn and Kollias, 2012). Z_e and v_m can be obtained as follows:

$$Z_e = 10^{18} \frac{\lambda^4}{\pi^5} |K|^2 \int \eta(v) dv; \quad (8)$$

$$v_m = \frac{\lambda \int \eta(v) v dv}{2 \int \eta(v) dv}, \quad (9)$$

where λ is the radar wavelength and $\eta(v)$ represents the Doppler spectra. $|K|^2 = |m^2 - 1/m^2 + 1|^2$, where m is the complex refractive index of water. So, Z_e and v_m are measured values.

3. Data availability

The MRR instrument was installed in July 2014 and, at the time of writing, had been operating for more than two

years without any serious malfunction. The MRR product contains averaged data, processed data (instantaneous data) and raw spectra. The processed data and raw spectra comprise averages over 10 s, and the averages are calculated from approximately 78 instantaneous spectra. The averaged data are processed on the basis of an average of multiple raw spectra, and the averaging time is 60 s (Muller et al., 2010), which is also the temporal resolution. Our analysis used the averaged data at a height of 100 m of a single rainfall episode, which occurred from 0000–0550 UTC 15 February 2015.

Following the guidance provided in the METEK manual, the analysis only used data from gates 3 to 31, i.e., excluding the lowest two gates, while several simplifications were applied at these two lowest altitudes.

4. Data analysis

In this section, the nature of the low-intensity precipitation properties of this single event with a BB is examined with the help of the MRR data. The variations in R , Z_e , v_m and GFV with altitude and time are analyzed, and methods to identify the BB and classify hydrometeors are proposed. Moreover, the DSD is analyzed in detail to understand the evolution of droplets by coalescence, break-up and evaporation.

4.1. Accuracy of the MRR data

To confirm the accuracy of the averaged data, the MRR products with a temporal resolution of 1 min were compared with in-situ disdrometer measurements. Due to a lack of disdrometer data during the selected precipitation event, another event that occurred on 29 June 2015 was analyzed. The disdrometer, as well as a laser-based optical disdrometer manufactured by Thies, was used for comparison. The Thies disdrometer is capable of measuring the diameter and velocity of droplets and, from these measurements, the R , Z and DSD can be calculated (Frasson et al., 2011). The R , Z and median volume diameter (D_0) were compared between the MRR and

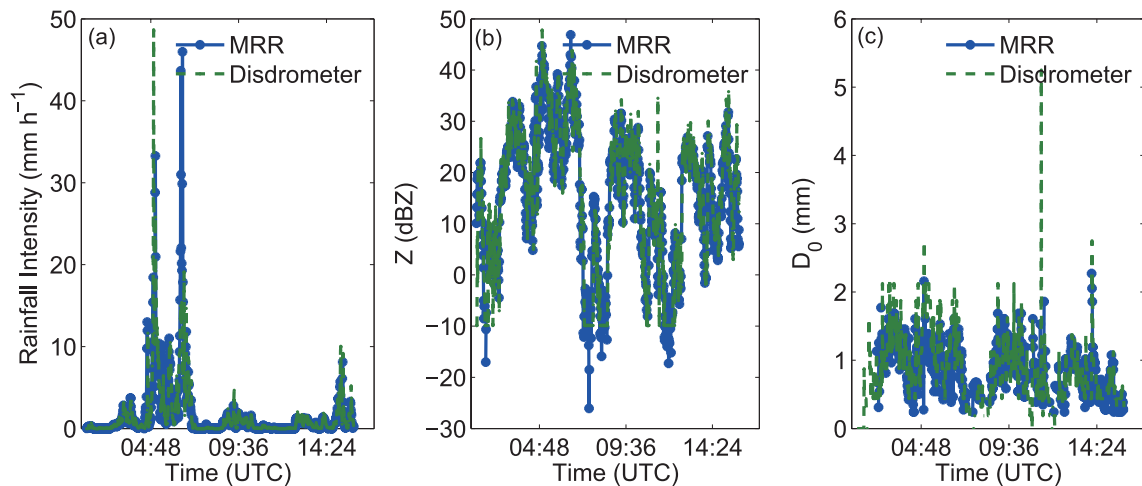


Fig. 1. Comparison between MRR and in-situ Thies disdrometers. The stratiform precipitation event occurred from 0118–1553 UTC 29 June 2015: (a) R ; (b) Z ; (c) D_0 .

disdrometer (Fig. 1), showing agreement. More specifically, the three parameters were highly consistent at low and moderate rainfall intensity but, for heavy rain, R and D_0 showed deviations.

4.2. Rain parameters

Throughout the entire precipitation process, the R was always below 2 mm h^{-1} at the height of 300 m (Fig. 2). The selected rain system was a typical stable stratiform precipitation event with characteristically wide horizontal ranges in contrast with its vertical height and weak vertical air motion. Cluckie et al. (2000) suggested that weak vertical air motion occurring in stable stratiform cloud is generated dynamically by turbulence or topography. Vertical air motion velocities are rarely greater than 1 m s^{-1} in a stratiform precipitation process (Cifelli and Rutledge, 1994; Konwar et al., 2012). As Cifelli and Rutledge (1994) pointed out, weak vertical drafts ($< 1 \text{ m s}^{-1}$) mean the presence of both mesoscale upward and downward motion with stratiform precipitation. Owing to its low intensity, the errors caused by the wind can be ignored. Besides, although several methods to estimate the vertical air motion from K-band precipitation spectra have been proposed (Rogers, 1964; Hauser and Amayenc, 1983), Peters et al. (2005) pointed out that the quality of these methods had not been assessed. Accordingly, Peters et al. (2005) compared these methods with vertical air motion measurements at a nearby tower and showed that the estimation error could be much larger than the actual vertical air motion. Vertical air motion “corrections” may even deteriorate the quality of precipitation parameters. Therefore, zero vertical air motion

was assumed in the present work.

The BB can be identified by the Z_e peak value below the 0°C isotherms shown in Fig. 3a. Maximum values of Z_e are found in the height range from 1400 m to 1900 m, as is apparent from Fig. 3a. Figure 3b shows the vertical temperature profile from a radiosonde station located approximately 50 km away from the MRR. These radiosonde data are observed at 0000 UTC and 1200 UTC every day. The selected MRR data began at 0000 UTC 15 February — the same time as the radiosonde observation. So, at the beginning of the precipitation process, the 0°C layer was at a height of 2000 m (shown in Fig. 3b). The freezing height from the radiosonde

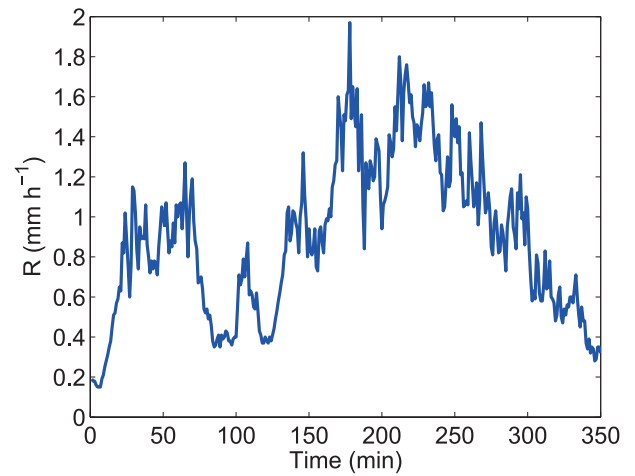


Fig. 2. Temporal evolution of R at 300 m; the R was always below 2 mm h^{-1} .

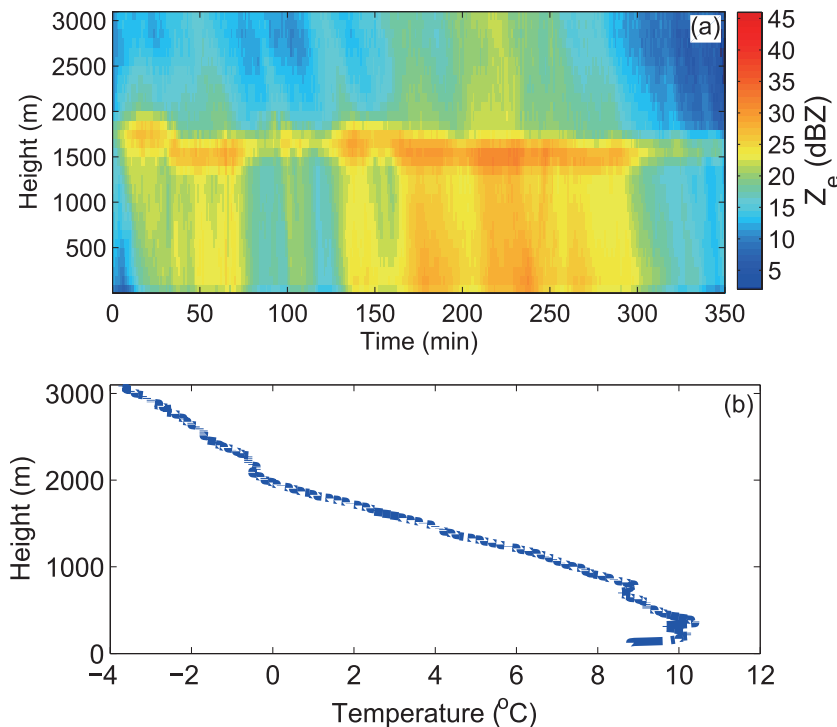


Fig. 3. (a) Time–height distribution of Z_e (units: dBZ). (b) Temperature profile from a radiosonde station located approximately 50 km away from the MRR, observed at 0000 UTC 15 February. The height of the 0°C layer is approximately 2000 m.

matched reasonably well with top of the BB in the MRR observation (Fig. 3a). By comparing the Z_e above and below the BB, the maximum reflectivity below the 0°C layer can be partly explained by the difference in the dielectric factor value between liquid water and ice (Cha et al., 2007). The radar reflectivity decreases as the particles fall below the BB because, when flakes melt into liquid droplets, the fall velocity increases, resulting in the number of particles decreasing per unit volume.

Figure 4 shows the variation of the retrieved fall velocity with time and height. The fall velocity increased at the bottom of the BB, with the maximum fall velocity appearing at around 1400 m and remaining unchanged as raindrops fell (Fig. 4), which reveals the occurrence of the liquid phase of water. Wegener (1911) proposed that the melting of ice particles generated raindrops. The fall velocity of the most dominant drop size remained the same below the BB. Hence, it can be assumed that the most dominant drop sizes that contributed to the R or LWC did not undergo a change.

4.3. DSD

To investigate the evolution of rain DSD by break-up, coalescence and evaporation, more details should be considered. In order to avoid the influence of ice-phase particles,

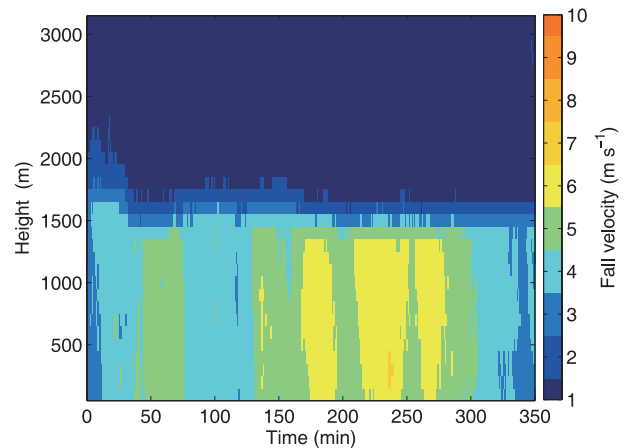


Fig. 4. Time–height distribution of fall velocity (m s^{-1}).

the DSD below the BB was analyzed. The time taken by raindrops from the BB to reach the ground was calculated. Below the BB (1400 m), the mean fall velocity of raindrops was 5.2 m s^{-1} . Consequently, most droplets took about 4.5 min to reach the ground. DSDs below the BB at a time interval of approximately 4 min [from the 25th to 28th minute (Figs. 5a–d)] are selected to illustrate the microphysics of pre-

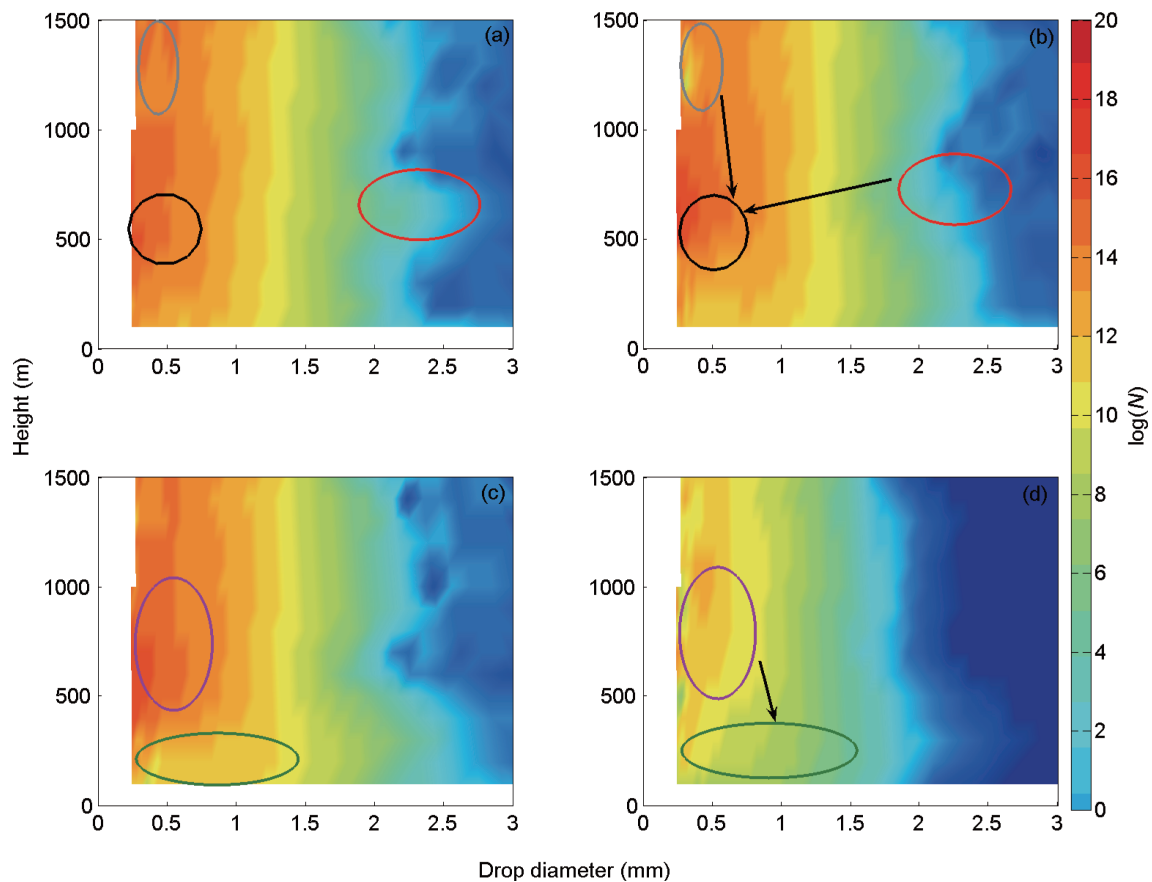


Fig. 5. The DSD (units: m^{-4}) at 4 min in 1 min steps: (a) 25th min; (b) 26th min; (c) 27th min; (d) 28th min. The number of drops of 1.6–2.5 mm in diameter decreased at a height of 700 m, marked with red circles, meanwhile, the smallest droplets decreased at heights of 1200–1500 m (gray circles), with a corresponding increase in smaller droplets (0.5–1 mm, black circles) at about 500 m, which may indicate break-up. DSD varied from regions marked with purple circles to green circles, which may indicate collision–coalescence and evaporation of small drops.

precipitation. The x -axis represents the droplet diameter, which ranges from 0.246 mm to 3 mm, the y -axis shows the height, and the logarithm of $N(D)$ is used on the z -axis. Here, the units of $N(D)$ are m^{-4} . In consideration of vertically slanted rain trails while rain falls from the BB bottom to the ground (Fabry and Zawadzki, 1995), there were no clear slanted rain trails from the top of the observing range to the ground in the time–height section of Z_e . So, it was unnecessary to consider the horizontal motion of the clouds producing vertically slanted rain trails. Droplets will fall at about 300 m min^{-1} , meaning droplets will have fallen about 300 m compared with the previous image. As shown in Fig. 5a, the number of smallest size class droplets varied from 13 to 18, which then varied from 10 to 18 in the next minute shown in Fig. 5b; that is, the $\log(N)$ of the smallest droplets decreased at heights of 1200–1500 m (gray circles) and below 400 m. Meanwhile, from Figs. 5a and b, we can see that the larger droplets at an altitude of about 700 m (diameter of 1.6–2.5 mm, represented by red circles) decreased with corresponding increases in the smaller droplets (0.5–1 mm, black circles) at about 500 m. We can also see the break-up of larger droplets (1.6–2.5 mm) at the height of 700 m and coalescence of droplets in the smallest size class at heights of 1200–1500 m from the 25th to 26th minute. As shown in Figs. 5b and c, the number of droplets varied from 0.5–0.8 mm in diameter at a height of about 750 m to 0.3–0.5 mm in diameter at a height of about 500 m, indicating the process of break-up of larger drops. It is apparent from Figs. 5c and d that coalescence and evaporation occurred with a decrease in small droplets (smaller than drops of 0.5 mm in diameter) at heights of 400–1000 m (marked with purple circles) and an increase in droplets of 0.5–1 mm in diameter below 500 m (green circles), in the same way. Also, the decrease in droplets may move out

of the radar beam owing to wind or turbulence. As shown from Fig. 5d, $\log(N)$ in the smallest size class was less than 18 mostly, which was smaller than the three minutes before (Figs. 5a–c). It is worth noting that the number of drops of 0.5–1 mm in diameter showed no noticeable variation below the BB throughout the whole rain episode. This may explain why the fall velocity was nearly constant below the BB (Fig. 4).

Figure 6 shows the DSD variations at six altitudes in 200 m steps below BB. As the rain drops fell from 1400 m to 400 m, the number of small particles decreased drastically, while the number of large particles increased (Figs. 6a–f). Theoretically, decreases in the number of smaller drops with corresponding increases in larger drops implies the existence of collision–coalescence. Conversely, decreases in the number of smaller drops observed without increases in larger drops indicates the possible occurrence of evaporation. In fact, as the rain drops fell from the BB bottom to the ground (Figs. 6a–f), they grew larger — chiefly by sweeping up other smaller drops, i.e., the collision–coalescence process. Meanwhile, the decrease in smaller droplets may also indicate evaporation (Figs. 6a–f). Muller et al. (2010) indicated that, in a stratiform precipitation event, evaporation would be happening as particles fall from the BB; and, during the evaporation process, small particles will evaporate preferentially (Muller et al., 2010). Therefore, the role of small droplets is to participate in the processes of collision–coalescence and evaporation.

Collision–coalescence and evaporation were the main microphysical processes during the whole rain event (Figs. 6a–f), although break-up could be observed in a few moments (Figs. 5a–d). Also, rain drops disintegrate once they reach a maximum size, which depends on the aerodynamically in-

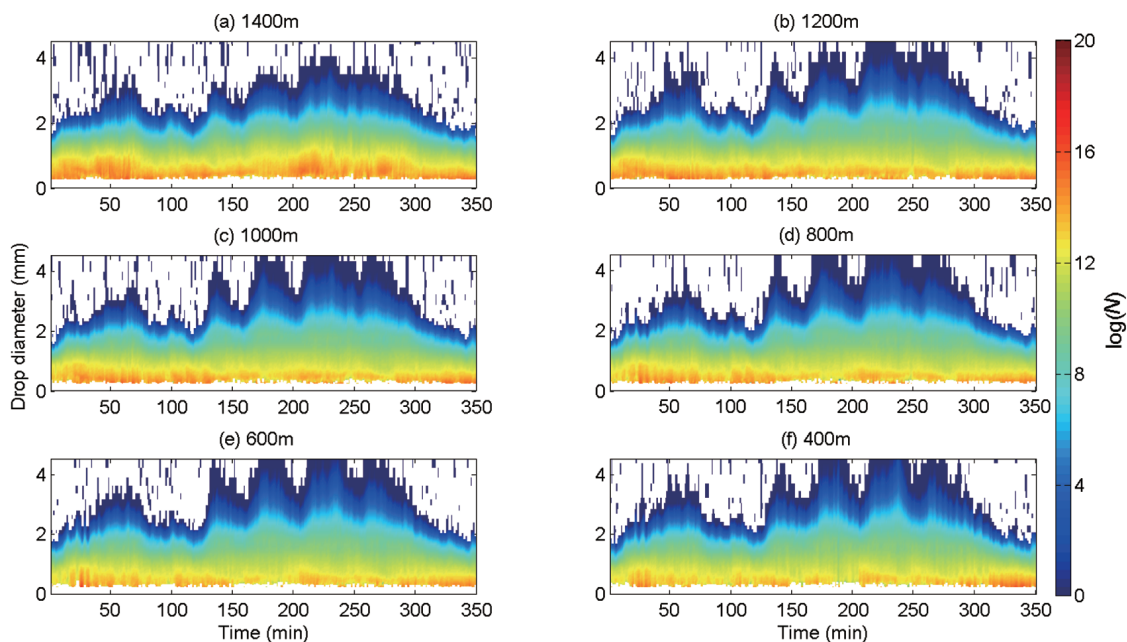


Fig. 6. The DSD (units: m^{-4}) variations at different altitudes: (a) 1400 m; (b) 1200 m; (c) 1000 m; (d) 800 m; (e) 600 m; (f) 400 m.

duced circulation of water in the drop, or, if they collide with other drops. This break-up produces more smaller drops, which themselves contribute to droplet growth and hence the break-up process again (Cluckie et al., 2000). A drop diameter of about 0.5–1 mm showed the same concentration at all heights, as indicated in Figs. 6a–f.

Since the vertical variation of the rain DSD in each minute was similar throughout the selected rain event, the data in the 100th minute are used as an example to illustrate the shape of the DSD below the BB. Figure 7 shows the shapes of the DSD at different altitudes from 300 m to 1400 m, in steps of 100 m. Each solid line represents the DSD at one particular altitude. The DSD at all heights behaved in a more or less similar manner (Fig. 7). As shown in Fig. 7, below the BB (below 1400 m), the DSD shows a Gamma distribution (Ulbrich, 1983). Therefore, we analyzed the correlation between the MRR DSD and fitted data.

The DSD below the BB was fitted to the Gamma distribution. A Gamma (Γ) distribution is formulated as follows (Ulbrich, 1983):

$$N(D) = N_0 D^\mu \exp(-\lambda D) \quad (10)$$

where N_0 is the intercept parameter, λ is the slope of the distribution, and μ is the shape parameter. Table 2 shows the fitting coefficients of the Gamma distribution and the goodness-of-fit below the BB height. The Gamma distribution more or less fitted the DSD below the BB. As can be seen from Table 2, the fitting coefficient N_0 varied between 36.27 and

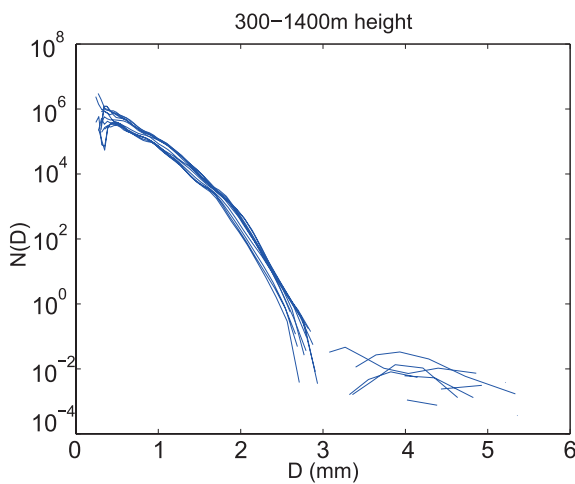


Fig. 7. Shape of the DSD (units: m^{-4}) in the 100th min below the BB.

74.12, μ varied from 0.55 to 1.22, while λ was approximately 1.5. The root-mean-square error (RMSE) was less than 2.5. The C value is a statistical value named the coefficient of multiple determination, which measures how close the fitted curve is in explaining the variation of the sampling data. The C value falls in the range between 0 and 1, with 1 indicating a perfect fit. As shown in Table 2, all the C values were close to 1 (greater than 0.83). A Gamma or Marshall–Palmer distribution (Marshall and Palmer, 1948) fitting bias is mainly caused by large droplets (Willis, 1984). Here, there were more larger droplets as rain fell, as shown in Fig. 6.

The correlation between the MRR-retrieved DSD and the theoretical DSD distribution was found to be generally good. Coalescence, break-up and condensation tend to produce an exponential distribution (Srivastava, 1971, 1978). Atlas et al. (2000) suggested that aggregation is the main process determining the stratiform DSD, backed up by the later work of Roy et al. (2005) and Muller et al. (2010). As seen from Fig. 6, coalescence may have been the dominant process behind the formation of the shape of the DSD.

4.4. Identification of the BB

A BB detection algorithm is proposed, and the advantages and drawbacks of the method are highlighted. Not only can the method retrieve the BB height, but it can also clearly reveal the evolution of the BB thickness with time.

Figure 8a shows the variation in GFV [$m\ s^{-1}\ (100\ m)^{-1}$] with time and height. The maximum GFV was at the bottom of the BB (Fig. 8a). The reason is that, as snowflakes fall across the $0^\circ C$ isotherm, they begin to melt inwards from their surface (White et al., 2002, 2003), and the velocity of the snowflakes increases. As the maximum radar reflectivity in the BB was in the region where ice-phase hydrometeors had not melted completely, it can be inferred that the droplet fall velocity would have continued to increase before melting into liquid water completely and reaching a maximum velocity. So, the maximal GFV appeared at the bottom of the BB, and the GFV could be used to identify the altitude of the BB bottom when enhanced Z_e was not prominent. The top of the BB could be derived from the gradient of the Z_e above the BB bottom. The BB thickness could then be calculated from the difference between the BB top height and BB bottom height:

$$BB_{\text{bottom}} = \max(\text{GFV}) ; \quad (11)$$

$$BB_{\text{top}} = \max(Z_{e(n+1)} - Z_{e(n)}) , \quad (12)$$

$$BB_{\text{thickness}} = BB_{\text{top}} - BB_{\text{bottom}} . \quad (13)$$

Table 2. Fitting coefficients of the Gamma distribution, and the goodness-of-fit, over the altitudinal range of 300 m to 1400 m.

	Height (m)											
	300	400	500	600	700	800	900	1000	1100	1200	1300	1400
N_0	51.77	57.89	63.39	74.12	59.10	36.27	56.56	48.55	45.89	45.00	45.14	49.98
μ	0.86	0.99	1.06	1.22	0.98	0.55	0.96	0.81	0.76	0.76	0.76	0.77
λ	1.55	1.64	1.71	1.85	1.64	1.17	1.56	1.40	1.35	1.33	1.34	1.45
RMSE	2.19	2.09	2.21	2.50	2.51	1.67	2.14	1.79	1.53	1.25	1.43	2.31
C	0.85	0.87	0.87	0.84	0.83	0.87	0.86	0.88	0.91	0.92	0.89	0.87

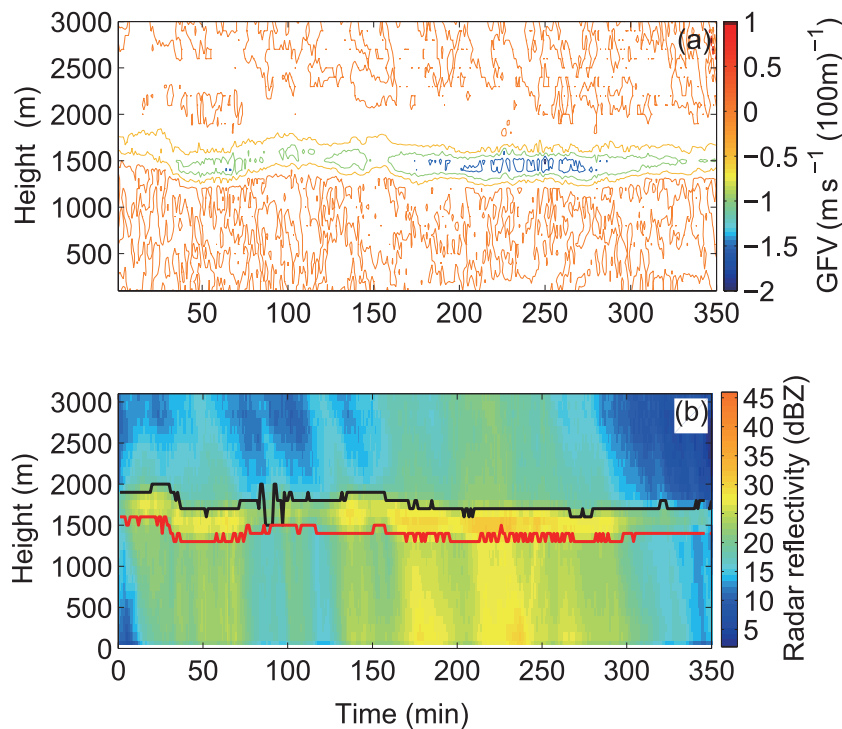


Fig. 8. (a) Time–height distribution of GFV [$\text{m s}^{-1} (100 \text{ m})^{-1}$]. (b) Time–height distribution of Z_e , in which the solid black line is the top of the BB retrieved by the gradient of Z_e , and the solid red line marks the bottom of the BB calculated by maximum GFV.

The BB top and bottom heights determined by the methods mentioned above, Eqs. (11)–(13) where $n = 1, 2, \dots, 30$ in Eqs. (12), are shown in Fig. 8. The algorithm appeared to identify the BB top and bottom heights correctly for most of the time on 15 February 2015, with only few outliers (Fig. 8). The GFV was a good indicator of the BB bottom, while the Z_e gradient signature was faint at the bottom of the BB, as revealed from Fig. 8b. The BB top height also indicated that the 0°C isotherm evolved with the precipitating system. The variation in BB thickness was captured successfully by the GFV together with the Z_e . Therefore, the MRR can provide a reliable and real-time estimation of the 0°C isotherm and BB thickness.

Nevertheless, there are some challenges involved in this method related to limitations of the algorithm and the parameter settings of the MRR. The BB top height is calculated based on the BB bottom height, so stable and accurate estimation of the BB bottom height is crucial for the BB top and thickness. The algorithm will be vulnerable if an erroneous estimation of the BB bottom height occurs at some point. A second challenge is that the altitudinal resolution and height range of the MRR parameters are contradictory. Here, to obtain a relatively high vertical resolution (100 m), the height range is only 3100 m, which will miss some BB detections while the BB height is above the height range, especially during the summer season. Huang et al. (2013) noted that the mean melting layer was from 3700 m to 5000 m in Beijing, China, from April to September 2010. So, adjusting the vertical resolution according to the seasons may be a feasible

approach to capturing more BB information.

4.5. Hydrometeor classification

As mentioned in section 4.1, the whole precipitation episode on 15 February 2015 was a liquid rain event on the ground. The BB (height range from about 1400 m to 1900 m) was in the melting layer, which leads us to ask: does the MRR have the potential to be used to classify the hydrometeors above the BB? Among all the retrieved parameters, the droplet fall velocity and Z_e , calculated by integrating the Doppler spectrum directly without estimating the liquid water, are two parameters that can be used. Accordingly, in this section, we attempt to use the droplet fall velocity to identify the types of snow crystals.

Figure 9 shows the droplet fall velocity at four altitudes above the BB: 2900 m, 2600 m, 2300 m, and 2000 m. It can be seen from Fig. 9 that the droplet fall velocity varied considerably at different altitudes in the first 30 min of the precipitation event. Specifically, it increased from 120 cm s^{-1} to 260 cm s^{-1} with a decrease in altitude from 2900 m to 2000 m. As shown in Fig. 3b, a change in temperature from -4°C to 0°C between 2900 m and 2000 m led to this variation. With the development of the precipitation system, the fall velocity at different heights decreased and then stabilized at approximately 120 cm s^{-1} . Nakaya and Terada Jr (1935) proposed a relationship between the dimension of snow particles and fall velocity through an experiment at Mt. Tokati. The fall velocities of needle, plane dendritic crystal, spatial dendritic crystal, and powder snow were no more than

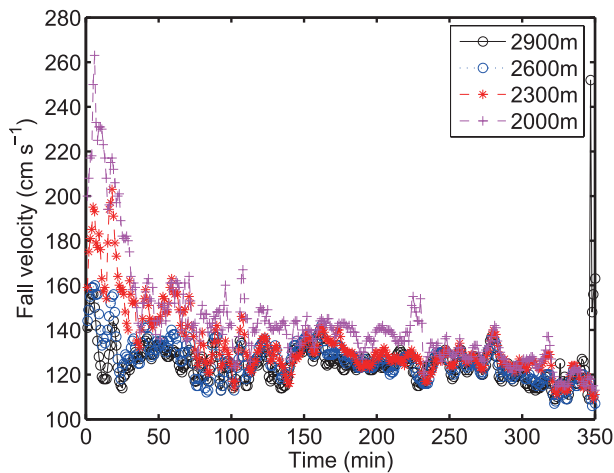


Fig. 9. Fall velocity of droplets at 2900 m (black line), 2600 m (blue line), 2300 m (red line), and 2000 m (magenta line).

80 cm s^{-1} . Meanwhile, the fall velocity of snow particles could vary from 80 cm s^{-1} to 120 cm s^{-1} , while the fall velocity of graupel (snow pellets) was in the range of $120\text{--}300 \text{ cm s}^{-1}$. All velocities of droplets exceeded 140 cm s^{-1} in the first 20 min of the precipitation event (Fig. 9), inferring graupel was prevalent during this period above the BB. Similarly, at 2000 m, graupel also dominated in the first 250 min. The riming process may lead to a fall velocity of less than 120 cm s^{-1} while supercooled water is attached to ice crystals. Of note is that the fall velocity at different heights was about 120 cm s^{-1} after 150 min of the development of the system, suggesting graupel and the riming process existed above the BB.

The 0000 UTC 15 February 2015 sounding also indicated the existence of the riming process above the BB, as shown in Fig. 3b. The vertical temperature profile finally warmed to 0°C at 2000 m, from which it was estimated that the 2000 m to 3000 m height layer was a mixed-phase layer, featuring the coexistence of supercooled water and ice crystals. This verifies the above inference: the main microphysical process above the BB was supercooled water condensing on the surface of the snow crystals, i.e., the riming process (Zawadzki et al., 2005; Konwar et al., 2012), generating graupel and dendritic crystals with water droplets.

5. Discussion and conclusions

In this study, we examined the evolution of the microphysical processes in a low-intensity rain event that occurred from 0000 to 0550 UTC on 15 February 2015 and featured a BB. On account of the low intensity, errors caused by vertical air motion could be ignored. The BB was identified by the enhanced radar reflectivity below the 0°C isotherm. Below the BB, the number of drops of $0.5\text{--}1 \text{ mm}$ in diameter showed no noticeable variation, so less spread was found in the fall velocity of the drops. According to Low and List (1982a, 1982b), drops smaller than 0.6 mm in diameter will only coalesce with larger drops when colliding. This might

indicate that the coalescence of smaller drops was more probable than disruption during collisions. As the rain fell to the ground, the number of smaller particles decreased, while the number of larger particles increased, indicating coalescence and evaporation. The microphysical processes (coalescence, break-up, evaporation) dominated the evolution of the DSDs. Below the BB, the DSD showed a Gamma distribution. The correlation between the MRR-retrieved DSD and the theoretical DSD distribution was found to be generally good.

The maximum velocity and the maximum GFV appeared at the bottom of the BB. Meanwhile, it was established that the GFV and reflectivity could be used to identify the altitude and the thickness of the BB. The BB top height is calculated based on the BB bottom height; therefore, accurate estimation of the BB bottom height is crucial for identifying the BB top and thickness. Moreover, not all BBs can be obtained by the MRR owing to the limitation of its height range. The altitudinal resolution is 100 m , while the height range of the MRR was 3100 m in this study. BB detections could be missed if the BB height is above the MRR height range, especially during the summer season. Therefore, adjusting the vertical resolution according to the seasons may be a feasible approach to capturing more information on the BB. Additionally, the MRR has its own advantages and limitations in terms of detecting BBs.

The droplet fall velocity was used to identify different types of snow crystals above the BB in this study. Above the BB ($2000\text{--}3000 \text{ m}$), there was a mixed-phase layer, i.e., the coexistence of supercooled water and ice crystals. The main microphysical process above the BB was riming. In the first 20 min of the selected stratiform precipitation event, graupel was prevalent above the BB. At 2000 m, graupel was also prevalent in the first 250 min. The fall velocity at different heights was about 120 cm s^{-1} after 150 min of the development of the system, inferring the existence of graupel and dendritic crystals with water droplets above the BB. The fall velocity of droplets is affected by the vertical air motion. Therefore, using the fall velocity for hydrometer classification may not be suitable for convective precipitation due to the large vertical air motion. In our selected precipitation event, vertical air motion was considered small and was neglected. As a measured parameter, fall velocity could be used for hydrometer classification for certain types of precipitation. As described in Ralph et al. (1995), for 404-MHz wind profiler radar, a downward fall velocity v of greater than $3\text{--}5 \text{ m s}^{-1}$ indicates rain; and snow is indicated by $0.5\text{--}0.9 \text{ m s}^{-1} < v < 2 \text{ m s}^{-1}$. The actual thresholds will vary with sustained upward or downward air motion; indeed, the thresholds of v have successfully identified snow in three widely differing situations (Ralph et al., 1995). Wang et al. (2014) analyzed the vertical beam data of Beijing wind profiler radar data, and found that the vertical velocity differed with different phases of water. The results indicated that vertical velocity has value in judging the phase of precipitation. The present study describes the microphysical properties of low-intensity precipitation featuring a BB by utilizing data captured by an MRR. It improves our understanding of

precipitation microphysics in eastern China. A full understanding of the cause of the variability requires a combination of more work using numerous observational instruments and numerical modeling. Meanwhile, more datasets could be used to analyze the microphysical processes of stratiform precipitation—not just one precipitation event. The different precipitation characteristics of stratiform, convective and mixed-type rain also need to be further researched.

Acknowledgements. This work was sponsored by the National Natural Science Foundation of China (Grant Nos. 41475028 and 41530427). The authors are grateful to Shandong Weather Modification Office, China, for assisting with maintaining the MRR instrument. The authors also wish to thank Dianli GONG, Dianguo ZHANG, Liming ZHOU and Qiuchen ZHANG for selecting and preparing the MRR data.

REFERENCES

- Atlas, D., R. C. Srivastava, and R. S. Sekhon, 1973: Doppler radar characteristics of precipitation at vertical incidence. *Rev. Geophys.*, **11**, 1–35, doi: 10.1029/RG011i001p00001.
- Atlas, D., C. W. Ulbrich, F. D. Marks, R. A. Black, E. Amitai, P. T. Willis, and C. E. Samsury, 2000: Partitioning tropical oceanic convective and stratiform rains by draft strength. *J. Geophys. Res.*, **105**, 2259–2267, doi: 10.1029/1999JD901009.
- Brandes, E. A., G. F. Zhang, and J. Vivekanandan, 2004: Drop size distribution retrieval with polarimetric radar: Model and application. *J. Appl. Meteor.*, **43**, 461–475, doi: 10.1175/1520-0450(2004)043<0461:DSDRWP>2.0.CO;2.
- Cha, J.-W., K.-H. Chang, S. S. Yum, and Y.-J. Choi, 2009: Comparison of the bright band characteristics measured by micro rain radar (MRR) at a mountain and a coastal site in South Korea. *Adv. Atmos. Sci.*, **26**, 211–221, doi: 10.1007/s00376-009-0211-0.
- Cha, J. W., S. S. Yum, K.-H. Chang, and S. N. Oh, 2007: Estimation of the melting layer from a micro rain radar (MRR) data at the cloud physics observation system (CPOS) site at daegwallyeong weather station. *Journal of the Korean Meteorological Society*, **43**, 77–85.
- Cifelli, R., and S. A. Rutledge, 1994: Vertical motion structure in maritime continent mesoscale convective systems: Results from a 50-Mhz profiler. *J. Atmos. Sci.*, **51**, 2631–2652, doi: 10.1175/1520-0469(1994)051<2631:VMSIMC>2.0.CO;2.
- Cluckie, I. D., R. J. Griffith, A. Lane, and K. A. Tilford, 2000: Radar hydrometeorology using a vertically pointing radar. *Hydrology and Earth System Sciences*, **4**, 565–580, doi: 10.5194/hess-4-565-2000.
- Das, S., A. K. Shukla, and A. Maitra, 2010: Investigation of vertical profile of rain microstructure at Ahmedabad in Indian tropical region. *Advances in Space Research*, **45**(10), 1235–1243, doi: 10.1016/j.asr.2010.01.001.
- Doelling, I. G., J. Joss, and J. Riedl, 1998: Systematic variations of Z–R-relationships from drop size distributions measured in northern Germany during seven years. *Atmospheric Research*, **47–48**, 635–649, doi: 10.1016/S0169-8095(98)00043-X.
- Fabry, F., and T. Zawadzki, 1995: Long-term radar observations of the melting layer of precipitation and their interpretation. *J. Atmos. Sci.*, **52**(7), 838–851, doi: 10.1175/1520-0469(1995)052<0838:LTROOT>2.0.CO;2.
- Foote, G. B., and P. S. Du Toit, 1969: Terminal velocity of raindrops aloft. *J. Appl. Meteor.*, **8**, 249–253, doi: 10.1175/1520-0450(1969)008<0249:TVORA>2.0.CO;2.
- Frasson, R. P. D. M., L. K. da Cunha, and W. F. Krajewski, 2011: Assessment of the Thies optical disdrometer performance. *Atmospheric Research*, **101**, 237–255, doi: 10.1016/j.atmosres.2011.02.014.
- Gossard, E. E., R. O. Strauch, and R. R. Rogers, 1990: Evolution of droplet size distributions in liquid precipitation observed by ground-based Doppler radar. *J. Atmos. Oceanic Technol.*, **7**, 815–828, doi: 10.1175/1520-0426(1990)007<0815:EODDIL>2.0.CO;2.
- Gunn, R., and G. D. Kinzer, 1949: The terminal velocity of fall for water droplets in stagnant air. *J. Meteor.*, **6**, 243–248, doi: 10.1175/1520-0469(1949)006<0243:TTVOFF>2.0.CO;2.
- Harikumar, R., S. Sampath, and V. S. Kumar, 2009: An empirical model for the variation of rain drop size distribution with rain rate at a few locations in southern India. *Advances in Space Research*, **43**, 837–844, doi: 10.1016/j.asr.2008.11.001.
- Harikumar, R., S. Sampath, and V. S. Kumar, 2010: Variation of rain drop size distribution with rain rate at a few coastal and high altitude stations in southern peninsular India. *Advances in Space Research*, **45**, 576–586, doi: 10.1016/j.asr.2009.09.018.
- Harikumar, R., S. Sampath, and V. S. Kumar, 2012: Altitudinal and temporal evolution of raindrop size distribution observed over a tropical station using a K-band radar. *Int. J. Remote Sens.*, **33**, 3286–3300, doi: 10.1080/01431161.2010.549853.
- Hauser, D., and P. Amayenc, 1983: Exponential size distributions of raindrops and vertical air motions deduced from vertically pointing Doppler radar data using a new method. *J. Climate Appl. Meteor.*, **22**, 407–418, doi: 10.1175/1520-0450(1983)022<0407:ESDORA>2.0.CO;2.
- Hu, Z. L., and R. C. Srivastava, 1995: Evolution of raindrop size distribution by coalescence, breakup, and evaporation: Theory and observations. *J. Atmos. Sci.*, **52**, 1761–1783, doi: 10.1175/1520-0469(1995)052<1761:EORSDB>2.0.CO;2.
- Huang, Y., Z. Ruan, R. S. Ge, J. L. Ma, and L. Ji, 2013: Feature statistics on bright band in Beijing in 2010 summer. *Meteorological Monthly*, **39**, 704–709, doi: 10.7519/j.issn.1000-0526.2013.06.006. (in Chinese)
- Kirankumar, N. V. P., and P. K. Kunhikrishnan, 2013: Evaluation of performance of Micro Rain Radar over the tropical coastal station Thumba (8.5°N, 76.9°E8). *Atmospheric Research*, **134**, 56–63, doi: 10.1016/j.atmosres.2013.07.018.
- Konwar, M., R. S. Mahes Kumar, S. K. Das, and S. B. Morwal, 2012: Nature of light rain during presence and absence of bright band. *Journal of Earth System Science*, **121**, 947–961, doi: 10.1007/s12040-012-0202-x.
- Low, T. B., and R. List, 1982a: Collision, coalescence and breakup of raindrops. Part I: Experimentally established coalescence efficiencies and fragment size distributions in breakup. *J. Atmos. Sci.*, **39**, 1591–1606, doi: 10.1175/1520-0469(1982)039<1591:CCABOR>2.0.CO;2.
- Low, T. B., and R. List, 1982b: Collision, coalescence and breakup of raindrops. Part II: Parameterization of fragment size distributions. *J. Atmos. Sci.*, **39**, 1607–1618, doi: 10.1175/1520-0469(1982)039<1607:CCABOR>2.0.CO;2.
- Maahn, M., and P. Kollias, 2012: Improved Micro Rain Radar snow measurements using Doppler spectra post-processing. *Atmospheric Measurement Techniques*, **5**, 2661–2673, doi: 10.5194/amt-5-2661-2012.

- Marshall, J. S., and W. M. Palmer, 1948: The distribution of raindrops with size. *J. Meteor.*, **5**, 165–166, doi: 10.1175/1520-0469(1948)005<0165:TDORWS>2.0.CO;2.
- METEK, cited 2017: MRR physical basics. Version 5.2.0.1, Metek mbH, Elmshorn, 20 pp. [Available online from <http://www.mpimet.mpg.de/fileadmin/atmosphaere/barbados/Instrumentation/MRR-physical-basics.20090707.pdf>]
- Muller, C. L., C. Kidd, I. J. Fairchild, and A. Baker, 2010: Investigation into clouds and precipitation over an urban area using micro rain radars, satellite remote sensing and fluorescence spectrophotometry. *Atmospheric Research*, **96**, 241–255, doi: 10.1016/j.atmosres.2009.08.003.
- Nakaya, U., and T. Terada Jr., 1935: Simultaneous observations of the mass, falling velocity and form of individual snow crystals. *Journal of the Faculty of Science, Hokkaido Imperial University. Series 2, Physics*, **1**(7), 191–200.
- Peters, G., B. Fischer, and T. Andersson, 2002: Rain observations with a vertically looking Micro Rain Radar (MRR). *Boreal Environment Research*, **7**, 353–362.
- Peters, G., B. Fischer, H. Münster, M. Clemens, and A. Wagner, 2005: Profiles of raindrop size distributions as retrieved by microrain radars. *J. Appl. Meteor.*, **44**, 1930–1949, doi: 10.1175/JAM2316.1.
- Peters, G., B. Fischer, and M. Clemens, 2010: Rain attenuation of radar echoes considering finite-range resolution and using drop size distributions. *J. Atmos. Oceanic Technol.*, **27**, 829–842, doi: 10.1175/2009JTECHA1342.1.
- Prat, O. P., and A. P. Barros, 2010: Ground observations to characterize the spatial gradients and vertical structure of orographic precipitation—Experiments in the inner region of the Great Smoky Mountains. *J. Hydrol.*, **391**, 143–156, doi: 10.1016/j.jhydrol.2010.07.013.
- Ralph, F. M., P. J. Neiman, D. W. Van de Kamp, and D. C. Law, 1995: Using spectral moment data from NOAA's 404-Mhz radar wind profilers to observe precipitation. *Bull. Amer. Meteor. Soc.*, **76**, 1717–1739, doi: 10.1175/1520-0477(1995)076<1717:USMDFN>2.0.CO;2.
- Rico-Ramirez, M. A., I. D. Cluckie, and D. Han, 2005: Correction of the bright band using dual-polarisation radar. *Atmospheric Science Letters*, **6**, 40–46, doi: 10.1002/asl.89.
- Rogers, R. R., 1964: An extension of the $Z-R$ relation for Doppler radar. *Proc. World Conf. Radar Meteorology and 11th Weather Radar Conf.*, Boulder, CO, Amer. Meteor. Soc., 158–161.
- Roy, S. S., R. K. Datta, R. C. Bhatia, and A. K. Sharma, 2005: Drop size distributions of tropical rain over south India. *Geofizika*, **22**, 105–130.
- Srivastava, R. C., 1971: Size distribution of raindrops generated by their breakup and coalescence. *J. Atmos. Sci.*, **28**, 410–415, doi: 10.1175/1520-0469(1971)028<0410:SDORGB>2.0.CO;2.
- Srivastava, R. C., 1978: Parameterization of raindrop size distributions. *J. Atmos. Sci.*, **35**, 108–117, doi: 10.1175/1520-0469(1978)035<0108:PORSD>2.0.CO;2.
- Ulbrich, C. W., 1983: Natural variations in the analytical form of the raindrop size distribution. *J. Climate Appl. Meteor.*, **22**, 1764–1775, doi: 10.1175/1520-0450(1983)022<1764:NVITAF>2.0.CO;2.
- Wang, L., G. R., Wang, Y. Gu, H. Y. Li, L. Ma, J. L. Guo, and L. Qiao, 2014: Application of wind profiler radar vertical radial velocity. *Meteorological Monthly*, **40**, 290–296, doi: 10.7519/j.issn.1000-0526.2014.03.004. (in Chinese)
- Wegener, A., 1911: Investigations on the nature of the upper atmosphere strata. I. *Phys Z*, **12**, 170–178.
- White, A. B., D. J. Gottas, E. T. Strem, F. M. Ralph, and P. J. Neiman, 2002: An automated brightband height detection algorithm for use with Doppler radar spectral moments. *J. Atmos. Oceanic Technol.*, **19**, 687–697, doi: 10.1175/1520-0426(2002)019<0687:AABHDA>2.0.CO;2.
- White, A. B., P. J. Neiman, F. M. Ralph, D. E. Kingsmill, and P. O. G. Persson, 2003: Coastal orographic rainfall processes observed by radar during the California land-falling jets experiment. *J. Hydrometeorol.*, **4**, 264–282, doi: 10.1175/1525-7541(2003)4<264:CORPOB>2.0.CO;2.
- Willis, P. T., 1984: Functional fits to some observed drop size distributions and parameterization of rain. *J. Atmos. Sci.*, **41**, 1648–1661, doi: 10.1175/1520-0469(1984)041<1648:FFTSOD>2.0.CO;2.
- Zawadzki, I., W. Szyrmer, C. Bell, and F. Fabry, 2005: Modeling of the melting layer. Part III: The density effect. *J. Atmos. Sci.*, **62**, 3705–3723, doi: 10.1175/JAS3563.1.